First-principles determination of the ultrahigh electrical and thermal conductivity in free-electron metals via pressure tuning the electron-phonon coupling factor

Ashutosh Giri, John T. Gaskins, Linqiu Li, Yi-Siang Wang, Oleg V. Prezhdo, and Patrick E. Hopkins

Phys. Rev. B **99**, 165139 — Published 25 April 2019

DOI: 10.1103/PhysRevB.99.165139

First principles determination of ultrahigh electrical and thermal conductivity in free electron metals via pressure tuning the electron-phonon coupling factor

Ashutosh Giri,[1,*] John T. Gaskins,[1] Linqiu Li,[2,3] Yi-Siang Wang,[2,3] Oleg V. Prezhdo,[2,3] and Patrick E. Hopkins[1,4,5,†]

[1]*Department of Mechanical and Aerospace Engineering, University of Virginia, Charlottesville, Virginia 22904, USA*

[2]*Department of Chemistry, University of Southern California, Los Angeles, CA, USA 90089*

[3]*Department of Physics and Astronomy, University of Southern California, Los Angeles, CA, USA 90089*

[4]*Department of Materials Science and Engineering, University of Virginia, Charlottesville, Virginia 22904, USA*

[5]*Department of Physics, University of Virginia, Charlottesville, Virginia 22904, USA*

(Dated: April 2, 2019)

Abstract

Responses of materials at high pressures can reveal fundamental insights into properties of condensed matter that are otherwise masked under ambient conditions. Using first principles calculations to determine the electron-phonon interactions of free electron metals at high pressures, we show that the electrical and thermal transport properties of aluminum, gold, and silver can be significantly enhanced with the application of high pressures. This is partly attributed to the decrease in electron-phonon coupling with increasing pressures. At elevated temperatures, under these high pressure conditions, the thermal conductivity of aluminum is amongst the highest of any known material, surpassing the thermal conductivity of diamond at ambient pressure. Moreover, through calculation of the spectrally resolved electron-phonon coupling parameter at high pressures, we show that the contribution to electron-phonon coupling from high-frequency longitudinal phonon modes scattering with electrons is increased in aluminum while in gold and silver, low frequency acoustic phonons scattering with electrons are increased at higher pressures. This work provides valuable insights into the electron-phonon scattering processes occurring under high pressures, which gives rise to new regimes of electrical and thermal transport properties in metals.

I. INTRODUCTION

The proper description of the fundamental scattering processes and interactions between electrons and lattice vibrations can significantly advance the quantitative understanding of various physical phenomena such as superconductivity,[1,2] electrical and thermal resistivities,[3] spin caloritronics,[4,5] and laser induced phase transitions.[6–8] The ability to tune these physical properties over a wide range has received a great deal of attention. To this end, high pressure studies have shown the ability to effectively tune the thermal conductivity of various materials over different phases,[9–12] increase interfacial transport,[13,14] and change the superconducting transition temperatures even in elements that are not superconducting at ambient pressures,[15–17] thereby advancing our fundamental understanding of physical processes occurring in condensed matter. Inspite of the host of pressure dependent studies available, the understanding of electron-phonon (e-p) interactions and how energy exchange mechanisms between the electron and phonon subsystems affect transport properties in metallic elements under high pressure is not well understood.

At ambient pressures, first principles calculations based on linear response theory have shed light on mode-dependent e-p coupling in several elemental metals with good agreement between the theory and tunneling experiments.[18–20] Since the early works by Kaganov *et al.*,[21] Anisimov *et al.*,[22] and Allen *et al.*[23,24] that describe the energy exchange between the electronic and the vibrational states with a two-temperature approach, first principles calculations on metals have also shown that the volumetric energy transfer rate between electrons and the lattice can be significantly enhanced at elevated electron temperatures.[25,26] More recently, the lattice contribution to thermal conductivity in metals has been predicted at intermediate temperatures by solving the Boltzmann Transport Equation (BTE) in conjunction with first principles calculations, which takes into account the e-p and phonon-phonon (p-p) contributions.[27,28] At high and low temperatures, however, the importance of electron-electron (e-e) scattering has also been emphasized in recent works.[29,30] Here, we are concerned with the intermediate temperature regime (100 K–700 K) for free electron metals, where electron-impurity and e-e scattering processes are less pronounced than e-p interactions and, thus, the e-p interactions poses the majority of the resistance to charge and heat flow.

The goal of this work is to predict the mode-dependent e-p coupling interactions under the application of large hydrostatic pressures for free electron metals (aluminum, gold, and silver) from *ab initio* calculations without adjustable parameters. From the results of our first-principles

calculations, we calculate the electrical and thermal conductivities for these three metals at high pressures and show that the comparatively larger decrease in e-p coupling scattering rates for Al, relative to those in Au and Ag, at high pressures can significantly increase the transport properties of Al more so than in Ag and Au. At large hydrostatic pressures, the reduction in the e-p coupling factor in these free electron metals leads to considerable increases in their resultant electrical conductivities and electron thermal conductivities. In particular, due to the large reduction in e-p coupling factor with increased pressure, we find that electron thermal conductivities in Al, Au, and Ag increase to values that rival the 'ultrahigh' phonon thermal conductivities in certain non-metals at room temperature. At elevated temperatures under these high pressure conditions, the thermal conductivity of aluminum is amongst the highest of any known material, surpassing the thermal conductivity of diamond measured at ambient pressures.

II. METHODOLOGY

The e-p scattering rates and coupling coefficients were calculated under the density functional perturbation theory as implemented in the Quantum Espresso package.[31] The measure of the likelihood of specific phonon modes with energy $\hbar\omega$ to scatter electrons from a particular state in the Fermi surface to another is given by the e-p spectral function or the Eliashberg transport coupling function $\alpha^2_{\rm tr}F(\omega)$. To calculate many thermodynamic and transport properties such as the superconducting transition temperature, superconducting gap, and electrical resistivity, the sum or average of the e-p coupling over all phonon wavevectors, $\mathbf{q}$ with branch index j, throughout the entire Brillouin zone (BZ) is needed, which is given as,[3]

$$\alpha^2_{\rm tr}F(\omega) = \frac{1}{N(\varepsilon_{\rm F})}\sum_{\mathbf{q}j}\sum_{\mathbf{k}nm}|g^{\mathbf{q}j}_{\mathbf{k}+\mathbf{q}m,\mathbf{k}n}|^2\delta(\hbar\omega-\hbar\omega_{\mathbf{q}j}) \\ \delta(\varepsilon_{\mathbf{k}n}-\varepsilon_{\rm F})\delta(\varepsilon_{\mathbf{k}+\mathbf{q}m}-\varepsilon_{\rm F})\eta_{\mathbf{k}+\mathbf{q}m,\mathbf{k}n}. \quad (1)$$

Here $\mathbf{k}$ is the electron wavevector, $N(\varepsilon_{\rm F})$ is the density of states (DOS) of electrons per spin at the Fermi level, and $g^{\mathbf{q}j}_{\mathbf{k}+\mathbf{q}m,\mathbf{k}n}$ is the e-p matrix elements quantifying the scattering of an electron at Fermi surface from the state $|\mathbf{k}n\rangle$ to the state $|\mathbf{k}+\mathbf{q}m\rangle$. The efficiency factor

$$\eta_{\mathbf{k}+\mathbf{q}m,\mathbf{k}n} = 1-\frac{\mathbf{v}_{\mathbf{k}n}\cdot\mathbf{v}_{\mathbf{k}+\mathbf{q}m}}{|\mathbf{v}_{\mathbf{k}n}|^2}, \quad (2)$$

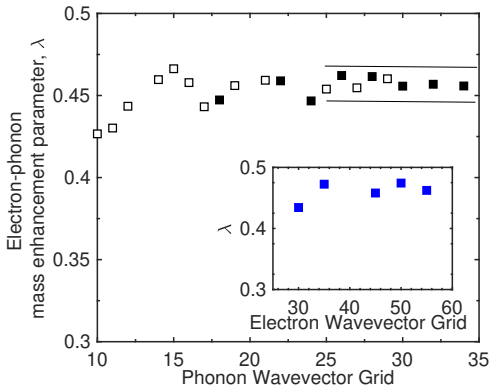

Figure 1. Electron-phonon mass enhancement parameter determined from first principles calculated on different phonon wave vector grid (for 30×30×30 (solid symbols) and 40×40×40 (hollow symbols) electronic wave vector grids) for Al. The black-line represent a 1 % variation in the mass enhancement parameter. (inset) Electron-phonon mass enhancement parameter determined from first principles calculated on different phonon wave vector grid for Al

which depends on the electron velocity $\mathbf{v}_{\mathbf{k}n}$ and accounts for the anisotropy by considering different scattering directions, is the difference between the transport spectral function defined in Eq. 1 and the spectral function, $\alpha^2F(\omega)$. Consequently, the e-p mass enhancement parameter (λ) and the transport constant ($\lambda_{\rm tr}$) that define the strength of e-p coupling are given as,

$$\lambda_{\rm (tr)} = 2\int_0^\infty \frac{\alpha^2_{\rm (tr)}F(\omega)d\omega}{\omega}. \tag{3}$$

For the accurate calculation of Eq. 1, a fine **k**-grid in the BZ is a prerequisite, which is efficiently computed within the framework of the electron-phonon Wannier (EPW) code.[32] Using the recently formulated maximally localized Wannier functions basis,[33] the e-p matrix elements, band energies, and phonon modes are interpolated from an initial coarse grid of 18×18×18 and 6×6×6 electron (**k**) and phonon wave vector grids (**q**), respectively, and interpolated to uniform grids of 40×40×40 and 30×30×30, for **k** and **q**, respectively, to conduct integration via the tetrahedron method. For our calculations, we use a plane wave energy cutoff of 816.3 eV (60 Ry) and a gaussian smearing of 0.34 eV (0.025 Ry).

Care must be taken to ensure that the interpolated fine grid of **k** and **q** points are dense enough for calculation of the converged values of e-p coupling coefficients. To check for convergence in the values of the calculated e-p mass enhancement parameter, λ, we performed calculations on dif-

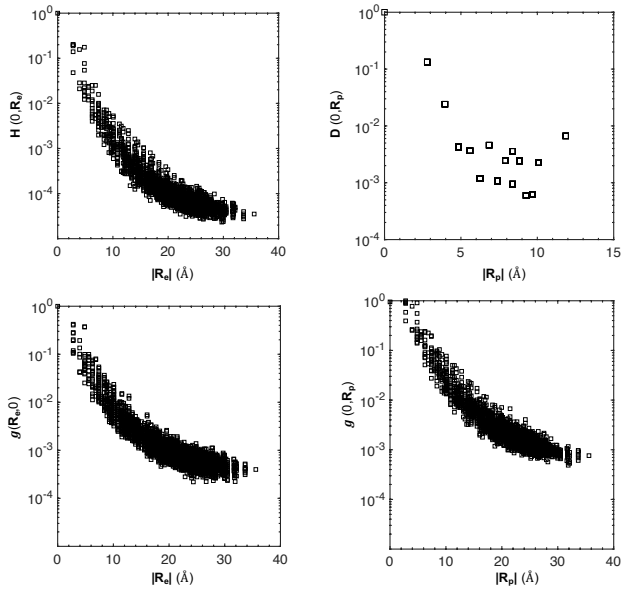

Figure 2. Spatial decays of the largest components of (a) the Hamiltonian $\mathbf{H}$, (b) the dynamical matrix $\mathbf{D}$ and the electron-phonon matrix elements (c) $\mathbf{g}(\mathbf{R_e}, \mathbf{0})$, (d) $\mathbf{g}(\mathbf{0}, \mathbf{R_p})$ for Al.

ferent combinations of wave vector grids for the electrons and phonons as shown in Fig. 1 where we plot λ versus the phonon wave vector grid size for Al. The hollow symbols represent calculations carried out on a 40×40×40 electronic wave vector grid, whereas, the solid symbols represent calculations carried out on a 30×30×30 electronic wave vector grid. As is clear, increasing the phonon grid size above 15×15×15 has less than 1 % change in the calculated λ. Along with that, the convergence of the data for the two electronic grid sizes also suggests that convergence has been reached in terms of the e-grid size. This is further solidified by the results presented in the inset of Fig. 1, which shows a constant value of λ for calculations performed on different e-grid sizes while a constant 30×30×30 phonon wave vector grid is used.

We further check for convergence of the electron and phonon wave vector grids along with the accuracy of the Wannier representation by confirming their localized nature; the spatial decay of the Hamiltonian, dynamical matrix, and the e-p coupling matrix elements to zero confirms the localization of the Wannier functions and validates their use for high-quality interpolation. We plot the spatial decays of the Hamiltonian, the dynamical matrix and the electron-phonon coupling matrix elements in the Wannier functions representation for Al in Fig. 2. The electron Hamiltonian is obtained as,

$$H^{\mathrm{el}}_{\mathbf{R}_e,\mathbf{R}'_e} = \sum_{\mathbf{k}} w_{\mathbf{k}} \mathrm{e}^{-i\mathbf{k}\cdot(\mathbf{R}'_e-\mathbf{R}_e)} U^{\dagger}_{\mathbf{k}} H^{\mathrm{el}}_{\mathbf{k}} U_{\mathbf{k}}, \tag{4}$$

where $w_{\mathbf{k}}$ is the weight of the $\mathbf{k}$ points, $\mathbf{R}_e$ is the electron unit-cell and the guage matrix $U_{\mathbf{k}}$ yields the transformation between Bloch eigenstates and maximally localized Wannier functions (MLWFs).[34,35]

The transformation of the dynamical matrix to real-space representation is carried out using,

$$D^{\mathrm{ph}}_{\mathbf{R}_p,\mathbf{R}'_p} = \sum_{\mathbf{q}} w_{\mathbf{q}} \mathrm{e}^{-i\mathbf{q}\cdot(\mathbf{R}'_p-\mathbf{R}_p)} \mathbf{e}_{\mathbf{q}} D^{\mathrm{ph}}_{\mathbf{q}} \mathbf{e}^{\dagger}_{\mathbf{q}} \tag{5}$$

where $w_{\mathbf{q}}$ is the weight of the $\mathbf{q}$ points, $\mathbf{e}_{\mathbf{q}}$ are the orthonormal eigenvectors of the dynamical matrix. Consequently, the e-p matrix elements are given as,

$$g(\mathbf{R}_e, \mathbf{R}_p) = \frac{1}{N_p} \sum_{\mathbf{q},\mathbf{k}} w_{\mathbf{q}} \mathrm{e}^{-i(\mathbf{k}\cdot\mathbf{R}_e+\mathbf{q}\cdot\mathbf{R}_p)} U^{\dagger}_{\mathbf{k+q}} g(\mathbf{k},\mathbf{q}) U_{\mathbf{k}} \mathbf{u}^{-1}_{\mathbf{q}}, \tag{6}$$

Here, $U_{\mathbf{k}}$ and $U_{\mathbf{k+q}}$ are the electronic matrices, $\mathbf{u}_{\mathbf{q}}$ are the phonon eigenvectors scaled by the atomic masses, and N_p is the number of unit cells in the period supercell.[34,35] As is clear from Fig. 2, all quantities decay to zero very quickly with distance in the electron or phonon unit cells, which suggests that high quality interpolation has been achieved via the MLWFs. Note, the phonon frequencies and band energies obtained via the interpolation agree with those calculated directly by the density functional theory calculations and also agree with previous works,[19,20,28,36] which provides confidence in our approach for calculating the e-p coupling matrix elements at high pressures (as will be detailed below).

III. RESULTS AND DISCUSSIONS

Figure 3 shows our results of the electronic structure calculations for the electron DOS at three different pressures for the metals considered in this work. The application of hydrostatic pressure reduces the unit cell size and leads to band broadening for all three metals. The DOS at the Fermi level, $N(\varepsilon_{\mathrm{F}})$, is lowered monotonically with increasing pressure, as seen clearly for the case of Al in Fig. 3a. The large density of states of d bands in Au and Ag mask this decrease of $N(\varepsilon_{\mathrm{F}})$ (Figs. 3b and 3c), however, as shown in the insets of Figs. 3b and 3c, there is indeed a monotonic decrease in $N(\varepsilon_{\mathrm{F}})$ with pressure for the noble metals as well.

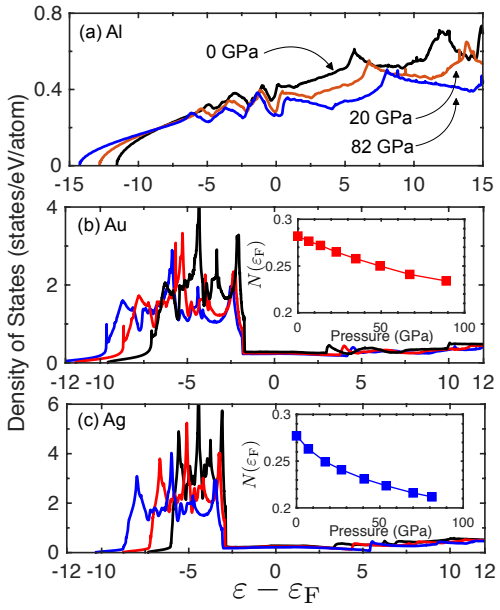

Figure 3. The electronic structure calculations of the electronic density of states for (a) Al, (b) Au, and (c) Ag at three different pressures. The insets show the evolution of density of states at the Fermi level, $N(\varepsilon_{\mathrm{F}})$ for (b) Au and (c) Ag. The application of hydrostatic pressure monotonically reduces $N(\varepsilon_{\mathrm{F}})$ for all three metals.

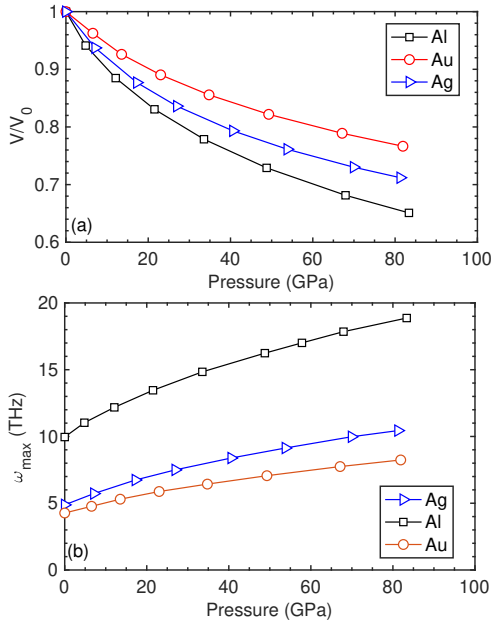

Figure 4. (a) The relative change of volume as a function of pressure for Al, Au and Ag. (b) Maximum phonon frequency vs. pressure for Al, Au and Ag.

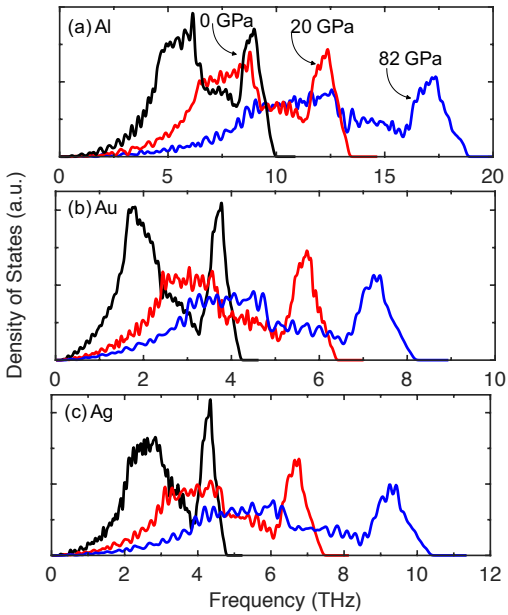

Figure 5. Density functional theory-calculated phonon density of states for (a) Al, (b) Au, and (c) Ag at three different pressures. The application of hydrostatic pressure monotonically increases the maximum phonon frequency due to lattice stiffening.

The application of hydrostatic pressure also causes the lattice to stiffen causing the spring constant that holds the atoms in their equilibrium position to increase; the increase in the spring constant is reflected by the positive curvature of the relative volume decrease with increasing pressure as shown in Fig. 4a where we plot the relative change in the volume as a function of pressure for Al, Au and Ag. As the bulk modulus of Al is lower than that compared to Au and Ag, a larger change in the volume with pressure is observed for Al in comparison to the noble metals. The positive curvature of the relative volume change suggests that the bonds stiffen and consequently the frequencies increase with the application of pressure for the pressure range studied in this work. This is shown in Fig. 4b where we plot the maximum phonon frequency for the three metals as a function of pressure. The maximum frequency in all three metals monotonically increases with pressure.

The increase in the spring constant is also reflected by the hardening of the phonon modes as shown in Fig. 5 at three different pressures. As mentioned above, the maximum frequency monotonically increases with pressure (see Fig. 4b) and the heights of the high-frequency peaks in the DOS also decrease with increasing pressure.

We also calculate the band structures of the three metals along high symmetry directions in

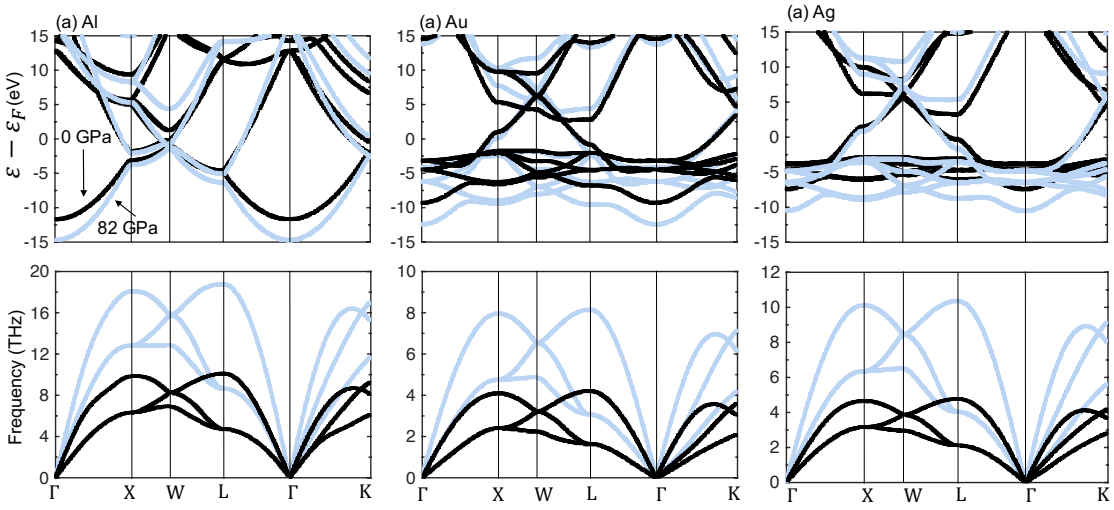

Figure 6. Band structures (top panels) and phonon dispersions (bottom panels) of (a) Al, (b) Au and (c) Ag along the high symmetry directions for ambient and high pressures.

Table I. Electron-phonon mass enhancement parameters (λ and $\lambda_{\rm tr}$) and the experimentally determined λ for Al, Au, and Ag. For comparison, we have also listed the values of λ and $\lambda_{\rm tr}$ at the highest pressure considered in this work.

	λ	$\lambda_{\rm tr}$	$\lambda_{\rm exp}$	λ (82 GPa)	$\lambda_{\rm tr}$ (82 GPa)
Al	0.46	0.39	0.38–0.48 (Ref. 3)	0.12	0.09
Au	0.22	0.21	0.12–0.22 (Ref. 3)	0.1	0.1
Ag	0.16	0.15	0.09–0.17 (Ref. 3)	0.074	0.072

the Brillouin zone as shown in Fig. 6. At ambient pressure, the band structures agree with previous DFT calculations. The effect of pressure is shown to broaden the energy spectrum for all three metals as shown in Fig. 6. Along with the electronic band structures, we also calculate the corresponding phonon dispersions (as shown in the bottom panels of Fig. 6) at the two extreme pressures considered in our work. Similar to the electronic spectrum, the effect of pressure is shown to broaden the phonon spectrum to higher frequencies for all phonon branches. We note that our lattice dynamics results for the phonon dispersions and DOS calculated at ambient pressure agree very well with prior works.[26,37]

Figures 7a, 7b, and 7c show the calculated e-p spectral functions, $\alpha^2F(\omega)$ (left panels) and e-p transport spectral functions, $\alpha^2_{\rm tr}F(\omega)$ (right panels) at three different pressures for Al, Au, and Ag,

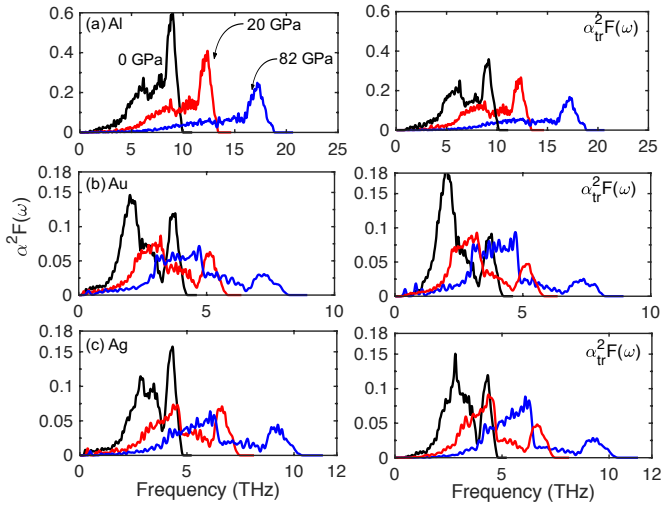

Figure 7. Calculated Eliashberg spectral functions $\alpha^2F(\omega)$ (left panels) and $\alpha^2_{\rm tr}F(\omega)$ (right panels) for (a) Al, (b) Au, and (c) Ag at three different pressures.

respectively. The corresponding mass enhancement parameters (λ) calculated via Eq. 3 at ambient pressure for Al, Au, and Ag are λ = 0.46, 0.22, and 0.16, respectively, which are in close agreement to those reported by prior works.[3,24] For comparison, the values for $\lambda_{\rm tr}$ for the three metals at the two extreme pressures considered in this work are also given in Table I. Our calculated $\alpha^2F(\omega)$ for Al are in good agreement with tunneling spectroscopy data as shown in Fig. 8a.[38] Tunneling data for nonsuperconductors are unavailable, however, our calculated $\alpha^2F(\omega)$ for Au shows good qualitative agreement with data obtained from point-contact spectroscopy (see Fig. 8b). For comparison, the density of states of the metals are also shown in the background of the figures. For Al, even though the experimental data agree very well with our calculations for $\alpha^2F(\omega)$, the high frequency contributions are considerably reduced for our calculations of $\alpha^2_{\rm tr}F(\omega)$. This is also evident from the values of the mass enhancement parameters λ and $\lambda_{\rm tr}$ for Al as listed in Table I, where the calculated $\lambda_{\rm tr}$ is $\sim$15 % lower than the value of λ at ambient, consistent with prior calculations of DFT-based linear-response theory for Al in Ref. 20. Contrastingly, for the noble metals, the values of λ and $\lambda_{\rm tr}$ are similar. Therefore, accounting for anisotropy in the different scattering directions can reduce the calculated e-p coupling strength in Al, whereas, for the noble metals, the peaks in $\alpha^2F(\omega)$ shift to lower frequencies in (as shown in Figs. 7b and 7c) without impacting the overall e-p coupling strength.

Considering the phonon DOS, $F(\omega)$, apart from the phonon bandwidths in the three metals

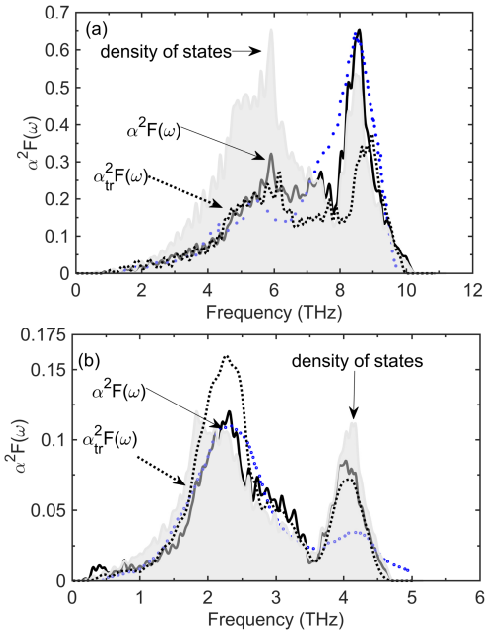

Figure 8. Calculated electron-phonon spectral functions of (a) Al and (b) Au along with experimental data (blue squares; taken from Refs. 39 and 38) and density of states plotted for reference. The dashed lines represent the transport spectral function, $\alpha^2_{\rm tr}F(\omega)$.

(Al has a much larger cutoff frequency of ∼17 THz compared to ∼4 and ∼5 THz in Au and Ag, respectively), the features of the phonon DOS for these metals are quite similar as shown in Fig. 5. Contrastingly, there are remarkable differences in their spectral functions. For Al, the spectral function shows a high frequency peak suggesting that longitudinal phonons in Al are coupled more strongly to electrons and contribute substantially to the overall λ (see Fig. 7a), which is consistent with the results from earlier works.[19,20,40] Whereas, comparatively in Au and Ag, the low-energy transverse phonons contribute more towards the e-p scattering processes as shown in Figs. 7b and 7c.

To show this more quantitatively, we calculate the accumulation function, $\lambda_{\rm tr}(\omega) = \int_0^\omega \alpha^2_{\rm tr}F(\omega)\omega^{-1}d\omega$, to investigate the spectral strength of e-p coupling in the three metals. In Fig. 9a, we plot accumulation of λ and $\lambda_{\rm tr}$ as a function of $\omega/\omega_{\rm max}$ for the three metals. In the case of Al, the reduction in the contributions from higher frequencies leads to an overall reduction in the value of $\lambda_{\rm tr}$, whereas, for Au and Ag, the λ and $\lambda_{\rm tr}$ are very similar (see also Table I) as mentioned above. In Fig. 9b, we plot the normalized accumulation of $\lambda_{\rm tr}$ vs. $\omega/\omega_{\rm max}$ to highlight the contribution from frequencies below the cutoff frequency of the transverse phonons (as denoted by the dashed lines). These

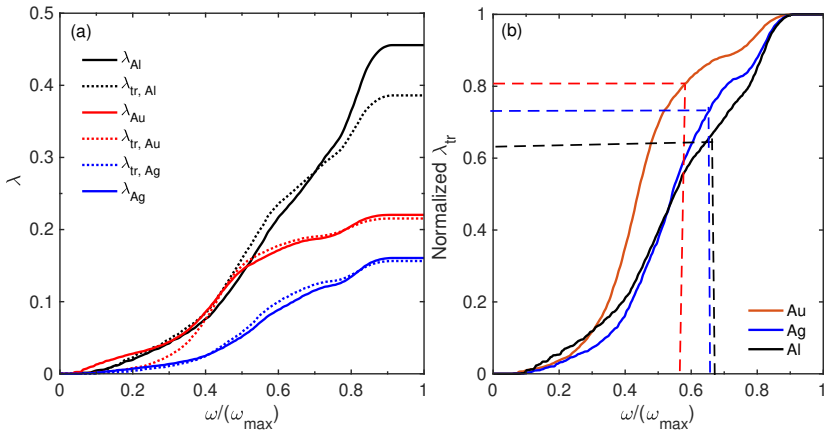

Figure 9. (a) $\lambda_{\rm tr}$ (dashed lines) and λ (solid lines) vs. $\omega/\omega_{\rm max}$ for Al, Au, and Ag. (b) Normalized $\lambda_{\rm tr}$ vs. $\omega/\omega_{\rm max}$ for the three metals, highlighting the contributions from frequencies lower than the cutoff frequency of the transverse phonons in each metal.

frequencies contribute $> 80\%$ to $\lambda_{\rm tr}$ for Au, while the contributions are relatively reduced for Al ($\sim$60%) and Ag ($\sim$70%), suggesting that transverse modes are better coupled to the electrons in Au more-so than in Ag and Al. Alternatively stated, our results suggest that the transverse modes in Au and Ag are coupled more strongly to their electrons than the corresponding process in Al.

While the phonon DOS and the dispersion relations (see Fig. 6) for the three metals are very similar (albeit with different cutoff frequencies), the electronic structures of the noble metals in comparison to that of Al are vastly different; the noble metals possess d bands lying within a few eV of the conduction band, whereas, Al has a free-electron-like electronic structure. The reason for the relatively larger coupling of transverse phonons to electrons in noble metals may be caused by the coupling of high energy d band electrons to the transverse modes.[41] These results are in contrast to several works that allude to the fact that electrons are more strongly scattered by longitudinal phonons.[42–45] It is also worth noting that the main features in the spectral functions for all three metals are partly determined by the corresponding phonon DOS, however, the spectral functions are shifted to higher frequencies in comparison to their respective DOS. This is more pronounced for the case of Al, as mentioned above, which points to the strong nonequilibrium (more so in Al than in Ag and Au) between the phonon states as the occupation of high-energy phonons is comparatively lower in a thermal state.

For all metals, the application of hydrostatic pressure causes the spectral functions to shift towards higher frequencies with notable reductions in their spectral peaks, similar to the changes ob-

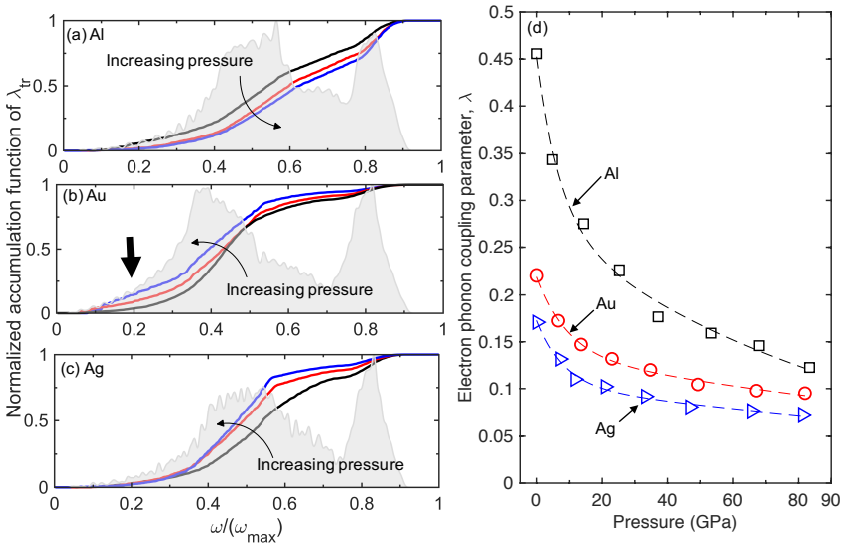

Figure 10. Normalized accumulation function of electron-phonon transport coupling strength as a function of normalized frequency for (a) Al, (b) Au and (c) Ag at the three different pressures. The arrows indicate the effect of increasing pressure and the bold arrow in (b) highlights the significantly higher contribution of lower frequency modes in Au as compared to that in Al and Ag. (d) Integrated electron-phonon coupling parameter λ versus applied hydrostatic pressures for the three metals calculated via Eq. 3.

served in their corresponding phonon DOS. To investigate and compare the effect of high pressures on the spectral e-p coupling in detail, we plot the normalized accumulation function for $\lambda_{\rm tr}(\omega)$ for the three metals as a function of their phonon frequencies normalized by their respective maximum frequencies in Figs. 10a, 10b and 10c. The DOS for the respective metals are also shown in light-gray scale in the background of the figures for reference. At ambient conditions, the higher frequency longitudinal phonons ($\gtrsim$7 THz) in Al contribute $\sim$40 % to the e-p coupling, whereas, the higher frequency longitudinal modes contribute $\sim$20 % and $\sim$30 % in Au and Ag, respectively. In comparison to both Al and Ag, the contribution from low frequency acoustic phonons in Au is larger as mentioned above. The application of higher pressures drastically increases this contribution for Au compared to the other two metals as seen in Fig. 10b. The application of pressure is also shown to shift the contribution in Al to higher frequencies, whereas, in the noble metals, the relative contributions are red shifted as indicated by the arrows in Figs. 10a, 10b and 10c. These findings suggest that the application of hydrostatic pressure tends to favor the phonon frequencies that dominate the e-p scattering mechanisms in these metals and the spectral dependencies

for each metal vary drastically between one another even though their phonon dispersions or even their electronic band structures are very similar as in the case of Ag and Au.

The corresponding calculations for λ as a function of pressure are shown in Fig. 10d for the three metals. The overall effect of pressure is shown to reduce the coupling between the two subsystems, however, it is interesting to note that $\sim$50 % reduction in the absolute values of λ can be achieved at $\sim$20 GPa, whereas, the application of higher pressures of up to $\sim$80 GPa only modestly decreases λ thereafter for all three metals. Another notable aspect of the results presented in Fig. 10d is the large difference in the values of λ between the noble metals and Al at ambient pressure, whereas, at higher pressures, the values are relatively similar for the three metals – the significance of which will be discussed in detail below.

We use the Eliashberg transport coupling function $\alpha^2_{\rm tr}F(\omega)$ calculated from the integral of the entire BZ to evaluate the electrical and thermal conductivities at high pressures. This allows us to gauge the relative effects of high pressures on the transport properties for the three metals considered in this work. As mentioned above, for the moderate temperature range that we are mostly concerned with in this work, e-p scattering is the dominant contribution to electrical resistivity while electron-electron scattering and electron-impurity scatterings can be neglected for reasonably pure metals. We use the lowest order variational approximation (LOVA) of the BTE to determine the electrical and thermal resistivities, which are given as,[3]

$$\rho(T) = \frac{4\pi m_e}{ne^2 k_{\rm B}T} \times \int_0^\infty \frac{\hbar\omega\alpha^2_{\rm tr}F(\omega)}{(\exp[\hbar\omega/k_{\rm B}T]-1)(1-\exp[-\hbar\omega/k_{\rm B}T])}d\omega, \tag{7}$$

$$\frac{1}{\kappa_e} = \frac{1}{L_0 T}\frac{4\pi m_e}{ne^2 k_{\rm B}T}\int_0^\infty \frac{\hbar\omega/d\omega}{(\exp[\hbar\omega/k_{\rm B}T]-1)(1-\exp[-\hbar\omega/k_{\rm B}T])} \times \left\{\left[1-\frac{1}{2\pi^2}\left(\frac{\hbar\omega}{k_{\rm B}T}\right)^2\right]\alpha^2_{\rm tr}F(\omega) + \frac{3}{2\pi^2}\left(\frac{\hbar\omega}{k_{\rm B}T}\right)^2\alpha^2F(\omega)\right\}, \tag{8}$$

where $k_{\rm B}$ is the Boltzmann constant, n is the number of electron per unit volume, e is the charge of an electron, m_e is the mass of an electron and L_0 is the Lorenz number, $(\pi^2/3)(k_{\rm B}/e)^2$. The expression for electrical resistivity is more popularly known as the Ziman's resistivity formula. It assumes that the phonons are in thermal equilibrium, the so called Bloch's *Annahme*, and is an excellent approximation for intermediate and high temperatures where phonon drag has negligible contributions to the resistivity. In deriving the LOVA for the resistivities, it is also assumed that

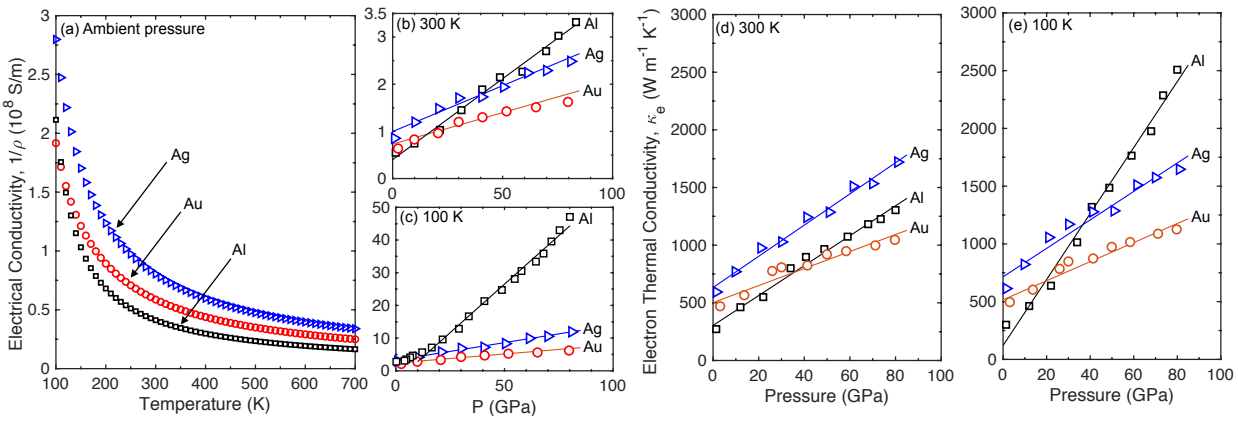

Figure 11. Calculated temperature dependence of electrical conductivity ($1/\rho(T)$) from the lowest-order variational solution of the Boltzmann transport equation for the three metals considered in this work. Electrical conductivities as a function of applied hydrostatic pressures at (b) 300 K and (c) 100 K. Electron thermal conductivities calculated from the spectral functions at (a) 300 K and (b) 100 K for the entire pressure range studied in this work.

the electron scattering rate ($\tau_{\mathbf{k},\varepsilon}$) is isotropic and energy independent, therefore, the expressions provide upper bounds for the resistivities. Note, our calculations for the Eliashberg coupling functions do take into account the e-p scattering processes occurring in the entire BZ.

In Fig. 11a, we plot the electrical conductivities ($1/\rho$) for the three metals calculated from Eq. 7 in the 100 to 700 K temperature range. Our results are in agreement with previous linear response theory calculations and are also in qualitative agreement with prior experimental results.[18,20,46] However, the use of the exact experimental lattice constant in the calculations can significantly improve the quantitative agreement between theoretically and experimentally determined electrical resistivities and also between the measured and predicted $\alpha^2_{\rm tr}F(\omega)$ as shown in Fig. 8.

We limit our calculations to moderate temperatures since at low temperatures ($T<\theta_D/5$, where θ_D is the Debye temperature), the sheets of Fermi surface displace independently and inelasticity corrections become important (as mentioned above, it is important to note that our calculations only take into account e-p scattering while impurity scattering and e-e scattering are neglected) and at high tempeartures ($T\gtrsim$1000 K), anharmonicity effects and Fermi-surface smearing need to be considered.[25,47,48] Consistent with previous experimental results,[46] our results show that at ambient pressure, Ag has the highest electrical conductivity of the three metals for the range of temperature studied (see Fig. 11a). The application of hydrostatic pressure monotonically increases the electri-

cal conductivity in all three metals as shown in Figs. 11b and c at 300 K and 100 K, respectively. The relative increase in conductivities with the application of hydrostatic pressure for Ag and Au are similar for the entire temperature range, whereas in Al, the conductivity increases rapidly with pressure and even surpasses that of Ag at $\sim$40 GPa at room temperature. The increase in the conductivity for Al is more pronounced at 100 K (as shown in Fig. 11c), where the conductivity of Al surpasses that of Ag at $\sim$10 GPa and is more than three times larger than that of Ag at $\sim$80 GPa. The higher increase in conductivity for Al is due to the fact that the differences between λ for the three metals at higher pressures is significantly reduced in comparison to the differences at ambient conditions (c.f. Fig. 10d) along with the fact that Al has a much higher electron number density amongst the three metals.

Figures 11d and e show the calculated electronic thermal conductivities at 300 K and 100 K, respectively. In contrast to the electrical conductivity, the thermal conductivity of Ag is higher than Al and Au at room temperature (Fig. 11e) for the entire pressure range studied in this work. However, the increase in the thermal conductivity with pressure for Al at 100 K is much larger amongst the three metals and at $\sim$40 GPa, the thermal conductivity of Al surpasses that of Ag. Moreover, at 100 K, the thermal conductivity of Al is $\sim$34 % and $\sim$55 % greater than that of Ag and Au, respectively, suggesting that the increased electron number density of Al relative to that of Au and Ag has a larger effect on thermal conductivity as compared to the decrease in e-p coupling with pressure at relatively low temperatures.

To compare the high electron thermal conductivities achieved via pressure tuning the e-p coupling factor of the three free-electron metals with other high thermal conductivity non-metals, in Fig. 12 we plot the temperature dependent thermal conductivity of Al at ambient, 30, and 82 GPa pressures along with those of other pertinent non-metals for which heat is predominantly transported by phonons. We also plot the experimentally determined thermal conductivity of Al (black circles), which agrees well with our calculations at ambient pressure. At room temperature and below, the thermal conductivity of Al at 82 GPa is comparable to that of the recently synthesized crystals of cubic boron arsenide (red and blue squares in Fig. 12). The thermal conductivity of diamond is higher than that of our pressurized Al at these temperatures, however, at higher temperatures, the thermal conductivity of Al at 82 GPa surpasses that of even diamond, which has the highest know thermal conductivity for a bulk solid. This is due to the fact that in semiconductors, anharmonic p-p scattering events increase with temperature, subsequently increasing the thermal resistivity. Therefore, at higher temperatures, while three phonon scattering lowers the

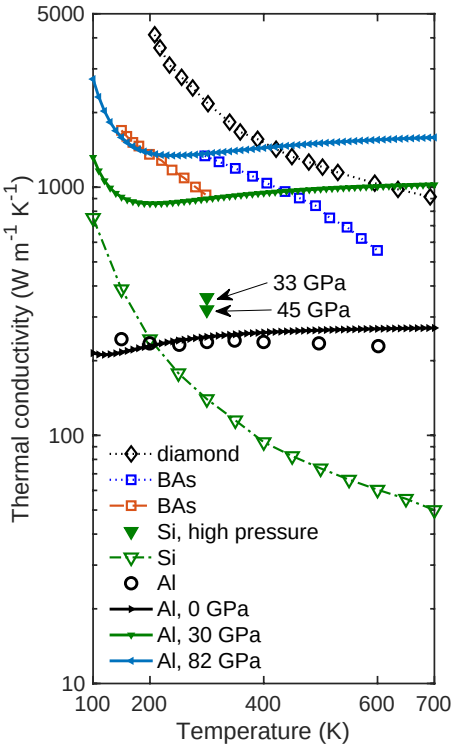

Figure 12. Calculated electron thermal conductivity vs. temperature for aluminum at 82 GPa (blue line), 30 GPa (green line), and ambient pressure (black line). For comparison, we also plot the measured temperature dependent thermal conductivity of non-metals such as diamond (diamond symbol; Ref. 49), boron arsenide measured by the steady-state method (red square symbols; Ref. 50) and the time domain thermoreflectance method (blue square symbols; Ref 51), and silicon (at ambient pressure shown by the green-hollow triangle symbols taken from Ref. 52 and at higher pressures shown by the green-solid triangle symbols taken from Ref. 12).

phonon-driven thermal conductivity, the electron-driven thermal conductivity slightly increases with temperature as shown in Fig. 12. As such, the electron-driven thermal conductivity of Al at high pressures is predicted to be much higher than those of the widely used high thermal conductivity semiconductors such as silicon carbide (which has a room temperature thermal conductivity of 490 W m^{-1} K^{-1}) and silicon (which has a room temperature thermal conductivity of 142 W m^{-1} K^{-1}, as shown in Fig. 12 by the hollow green triangle symbols). Furthermore, as reported in Ref. 12, the application of pressure (33 GPa) was shown to increase the thermal conductivity of

silicon by a factor of ∼2.3 (solid green triangles in Fig. 12) with a phase transition from diamond cubic to primitive hexagonal with metallic characteristics at high pressures. The authors reported that further compression to 45 GPa did not increase the thermal conductivity of metallic silicon. In contrast, our calculations show that the thermal conductivity of free electron metals monotonically increases (over the pressure range studied in this work). Moreover, compared to a modest increase by a factor of ∼2.3 (at 33 GPa) for silicon, the thermal conductivity of aluminum can be increased by a factor of ∼3.5 by increasing the pressure from ambient to ∼30 GPa.

IV. CONCLUSIONS

In summary, we employ first principles calculations to determine the e-p coupling matrix elements at high pressures. At large hydrostatic pressures, the reduction in the e-p coupling factor in these free electron metals leads to considerable increases in their electrical conductivities and electron thermal conductivities. In particular, due to the reduction in e-p coupling factor with increased pressure, we find that the electron thermal conductivities in aluminum, silver, and gold increase to values that start to rival the 'ultrahigh' phonon thermal conductivities in certain nonmetals at room temperature. At elevated temperatures, under these high pressure conditions, the thermal conductivity of aluminum is one of the highest of any known material, surpassing the thermal conductivity of diamond at ambient pressure. This is shown to be a consequence of a larger decrease in the e-p coupling parameter at higher pressures for aluminum compared to the decrease in the coupling parameters for gold and silver. Our calculations of the spectrally resolved e-p coupling reveals that the strength of high frequency longitudinal phonon modes coupling with electrons is increased in aluminum, whereas, low frequency acoustic modes coupling with electrons is favored in gold and silver at higher pressures. This study provides intricate insights into the fundamental scattering processes occurring in metals under high pressures, which reveals a wealth of understanding into the condensed state of free electron metals.

ACKNOWLEDGEMENTS

We would like to thank the Army Research Office for support under a MURI program (Grant No. W911NF-16-1-0406). This manuscript is based upon work supported by the Air Force Office

of Scientific Research under Award No. FA9550-18-1-0352.

---

* ag4ar@virginia.edu

† phopkins@virginia.edu

[1] P. B. Allen, Phys. Rev. Lett. **59**, 1460 (1987).

[2] W. L. McMillan, Phys. Rev. **167**, 331 (1968).

[3] G. Grimvall, Physica Scripta **14**, 63 (1976).

[4] G. E. W. Bauer, E. Saitoh, and B. J. van Wees, Nat Mater **11**, 391 (2012).

[5] J. Sinova, Nat Mater **9**, 880 (2010).

[6] W.-L. Chan, R. S. Averback, D. G. Cahill, and A. Lagoutchev, Phys. Rev. B **78**, 214107 (2008).

[7] W.-L. Chan, R. S. Averback, D. G. Cahill, and Y. Ashkenazy, Phys. Rev. Lett. **102**, 095701 (2009).

[8] D. S. Ivanov and L. V. Zhigilei, Phys. Rev. B **68**, 064114 (2003).

[9] D. A. Dalton, W.-P. Hsieh, G. T. Hohensee, D. G. Cahill, and A. F. Goncharov, **3**, 2400 EP (2013).

[10] B. Chen, W.-P. Hsieh, D. G. Cahill, D. R. Trinkle, and J. Li, Phys. Rev. B **83**, 132301 (2011).

[11] W.-P. Hsieh, M. D. Losego, P. V. Braun, S. Shenogin, P. Keblinski, and D. G. Cahill, Phys. Rev. B **83**, 174205 (2011).

[12] G. T. Hohensee, M. R. Fellinger, D. R. Trinkle, and D. G. Cahill, Phys. Rev. B **91**, 205104 (2015).

[13] G. T. Hohensee, R. B. Wilson, and D. G. Cahill, Nat Commun **6** (2015).

[14] W.-P. Hsieh, A. S. Lyons, E. Pop, P. Keblinski, and D. G. Cahill, Phys. Rev. B **84**, 184107 (2011).

[15] D. U. Gubser and A. W. Webb, Phys. Rev. Lett. **35**, 104 (1975).

[16] G. Profeta, C. Franchini, N. N. Lathiotakis, A. Floris, A. Sanna, M. A. L. Marques, M. Lüders, S. Massidda, E. K. U. Gross, and A. Continenza, Phys. Rev. Lett. **96**, 047003 (2006).

[17] J. Hamlin, Physica C: Superconductivity and its Applications **514**, 59 (2015), superconducting Materials: Conventional, Unconventional and Undetermined.

[18] S. Y. Savrasov, D. Y. Savrasov, and O. K. Andersen, Phys. Rev. Lett. **72**, 372 (1994).

[19] S. Y. Savrasov and D. Y. Savrasov, Phys. Rev. B **54**, 16487 (1996).

[20] R. Bauer, A. Schmid, P. Pavone, and D. Strauch, Phys. Rev. B **57**, 11276 (1998).

[21] M. Kaganov, I. Lifshitz, and L. V. Tanatarov, Sov. Phys. JETP **4**, 173 (1957).

[22] S. I. Anisimov, B. L. Kapeliovich, and T. L. Perelman, Sov. Phys. JETP **39**, 375 (1974).

[23] P. B. Allen, T. P. Beaulac, F. S. Khan, W. H. Butler, F. J. Pinski, and J. C. Swihart, Phys. Rev. B **34**, 4331 (1986).

[24] P. B. Allen, Phys. Rev. B **36**, 2920 (1987).

[25] Z. Lin, L. V. Zhigilei, and V. Celli, Phys. Rev. B **77**, 075133 (2008).

[26] A. M. Brown, R. Sundararaman, P. Narang, W. A. Goddard, and H. A. Atwater, Phys. Rev. B **94**, 075120 (2016).

[27] Y. Wang, Z. Lu, and X. Ruan, Journal of Applied Physics **119**, 225109 (2016), http://dx.doi.org/10.1063/1.4953366.

[28] A. Jain and A. J. H. McGaughey, Phys. Rev. B **93**, 081206 (2016).

[29] B. Y. Mueller and B. Rethfeld, Phys. Rev. B **87**, 035139 (2013).

[30] A. Giri and P. E. Hopkins, Journal of Applied Physics **118**, 215101 (2015).

[31] P. Giannozzi, S. Baroni, N. Bonini, M. Calandra, R. Car, C. Cavazzoni, D. Ceresoli, G. L. Chiarotti, M. Cococcioni, I. Dabo, A. D. Corso, S. de Gironcoli, S. Fabris, G. Fratesi, R. Gebauer, U. Gerstmann, C. Gougoussis, A. Kokalj, M. Lazzeri, L. Martin-Samos, N. Marzari, F. Mauri, R. Mazzarello, S. Paolini, A. Pasquarello, L. Paulatto, C. Sbraccia, S. Scandolo, G. Sclauzero, A. P. Seitsonen, A. Smogunov, P. Umari, and R. M. Wentzcovitch, Journal of Physics: Condensed Matter **21**, 395502 (2009).

[32] S. Poncé, E. Margine, C. Verdi, and F. Giustino, Computer Physics Communications **209**, 116 (2016).

[33] N. Marzari, A. A. Mostofi, J. R. Yates, I. Souza, and D. Vanderbilt, Rev. Mod. Phys. **84**, 1419 (2012).

[34] F. Giustino, M. L. Cohen, and S. G. Louie, Phys. Rev. B **76**, 165108 (2007).

[35] J. D. Noffsinger, *The Electron-Phonon Interaction from First Principles. [electronic resource].* (Berkeley, CA, 2011., 2011).

[36] S. Kupratakuln and G. C. Fletcher, Journal of Physics C: Solid State Physics **2**, 1886 (1969).

[37] J. W. Lynn, H. G. Smith, and R. M. Nicklow, Phys. Rev. B **8**, 3493 (1973).

[38] E. L. Wolf, *Principles of Electron Tunneling Spectroscopy* (Oxford University Press, 1985).

[39] A. G. M. Jansen, F. M. Mueller, and P. Wyder, Phys. Rev. B **16**, 1325 (1977).

[40] A. Y. Liu and A. A. Quong, Phys. Rev. B **53**, R7575 (1996).

[41] S. G. Das, Phys. Rev. B **7**, 2238 (1973).

[42] A. V. Sergeev and M. Yu. Reizer, International Journal of Modern Physics B **10**, 635 (1996).

[43] L. Waldecker, R. Bertoni, R. Ernstorfer, and J. Vorberger, Phys. Rev. X **6**, 021003 (2016).

[44] S. Ono, Phys. Rev. B **97**, 054310 (2018).

[45] H. Teichler, physica status solidi (b) **48**, 189 (1971).

[46] J. S. Dugdale and A. Myers, *Metals: Electronic Transport Phenomena*, edited by K. H. Hellwege and O. Madelung, New Series, Group III, Vol. 15c (Springer-Verlag Berlin Heidelberg, 1982).

[47] F. J. Pinski, P. B. Allen, and W. H. Butler, Phys. Rev. B **23**, 5080 (1981).

[48] A. M. Brown, R. Sundararaman, P. Narang, A. M. Schwartzberg, W. A. Goddard, and H. A. Atwater, Phys. Rev. Lett. **118**, 087401 (2017).

[49] J. R. Olson, R. O. Pohl, J. W. Vandersande, A. Zoltan, T. R. Anthony, and W. F. Banholzer, Phys. Rev. B **47**, 14850 (1993).

[50] F. Tian, B. Song, X. Chen, N. K. Ravichandran, Y. Lv, K. Chen, S. Sullivan, J. Kim, Y. Zhou, T.-H. Liu, M. Goni, Z. Ding, J. Sun, G. A. G. U. Gamage, H. Sun, H. Ziyaee, S. Huyan, L. Deng, J. Zhou, A. J. Schmidt, S. Chen, C.-W. Chu, P. Y. Huang, D. Broido, L. Shi, G. Chen, and Z. Ren, Science (2018).

[51] S. Li, Q. Zheng, Y. Lv, X. Liu, X. Wang, P. Y. Huang, D. G. Cahill, and B. Lv, Science (2018).

[52] W. Fulkerson, J. P. Moore, R. K. Williams, R. S. Graves, and D. L. McElroy, Phys. Rev. **167**, 765 (1968).